



# Fast Charge and High Stability of Solid-State Graphite Organic Ionic Plastic Crystal Composite Anodes

Hiroyuki Ueda,<sup>\*[a]</sup> Fuminori Mizuno,<sup>[b]</sup> Robert Kerr,<sup>[a]</sup> Maria Forsyth,<sup>[a]</sup> and Patrick C. Howlett<sup>\*[a]</sup>

All-solid-state batteries (ASSBs) using organic ionic plastic crystals (OIPCs) are promising candidates to overcome the inherent safety issues of lithium-ion batteries (LIBs). Although OIPCs have excellent process applicability in the roll-to-roll electrode fabrication process, their application as solid electrolytes incorporated in composite electrodes has yet to be demonstrated in detail. Herein, we denote the positive effect of the *N*-ethyl-*N*-methylpyrrolidinium bis(fluorosulfonyl)imide ( $[C_2mpyr][FSI]$ ) incorporated within a composite graphite anode on the charge rate capability and cycle life. The highest charge capacity ratio (the charge capacity at 2C vs. that measured at 0.1C) was measured for the composite anode with an OIPC composite ratio of 50 wt% (89.5%, 295.7 mAh/g at 2C charge), almost the same as that of the graphite anode with a liquid

electrolyte (85.7%, 295.9 mAh/g at 2C charge). More favorable lithium-ion conduction pathways were resolved for the anode with a higher OIPC composite ratio, whereas an excessive amount of OIPC reduced the long-term cyclability. The most stable discharge capacity retention was obtained for 30 wt% OIPC composite (257.4 mAh/g at the 100th discharge), which showed no signs of discharge capacity fading within 100 cycles. The lithiation/delithiation process of the solid-state graphite-[ $C_2mpyr][FSI]$  composite anode was evaluated to be stable and reversible. In addition, the incorporated OIPC composite enhanced the electrolyte/electrode and electrode/current collector contacts. This work highlights multiple advantageous functions of the OIPC in a composite graphite anode, which will broaden our horizons for the use of OIPC composites in ASSBs.

## Introduction

Since their first commercialization in 1991, lithium-ion batteries (LIBs) have been crucial components as energy-storage devices in many consumer electronics including, laptops and smartphones.<sup>[1]</sup> Demands for their large-scale utilization are ever growing along with a rapid expansion of the electric vehicles (EVs) market.<sup>[2]</sup> To extensively use LIBs in such a large-scale application, their safety must be ensured.<sup>[3]</sup> Current LIBs are fruits of manufacturers' labour and are practically safe as final products, which ensure sufficient precautions at each scale from optimization of cell chemistry to mechanical crash protection of battery modules.<sup>[4]</sup> However, at the cell-chemistry level, LIBs rely on flammable organic liquid electrolytes, posing

inherent safety risks. Therefore, all-solid-state batteries (ASSBs), in which solid electrolytes are used as ion-conductive pathways have attracted attention owing to the higher thermal stability of solid electrolytes compared to conventional liquid electrolytes in LIBs.<sup>[5]</sup> If ASSBs can be made cost-effective and achieve comparable performance with LIBs, the replacement of LIBs with ASSBs will be viable.

Another important factor is the process applicability of solid-state electrodes comprising active materials and solid electrolytes (plus, if necessary, conductive additives and binders) to current LIB production lines. Highly compatible preparation methods for the electrodes are beneficial to boost a wide adaptation of ASSBs in energy storage applications.<sup>[6]</sup> Although inorganic solid electrolytes are promising materials in terms of their bulk ionic conductivities, they require additional steps to form void-free contacts between the solid electrolytes and active materials.<sup>[3a,7]</sup> For instance, the interfacial formation of a sulfide-based solid electrolyte with  $LiNi_{1/3}Mn_{1/3}Co_{1/3}O_2$  requires high pressure (330 MPa) at room temperature,<sup>[8]</sup> whereas that of an oxide-based one with  $LiCoO_2$  is achieved at a high temperature (700 °C).<sup>[9]</sup> Such interfacial formation procedures cannot be directly performed in the roll-to-roll electrode fabrication process and, thus, increase costs for the mass production of ASSBs.<sup>[5a,10]</sup> In this context, organic solid electrolytes become attractive candidates because of their excellent process applicability,<sup>[11]</sup> for which current LIB fabrication technologies can be simply employed without implementing any additional low-throughput processes.

Among organic solid electrolytes, organic ionic plastic crystals (OIPCs) are an emerging class of ion conductors. They

[a] Dr. H. Ueda, Dr. R. Kerr, Prof. M. Forsyth, Prof. P. C. Howlett  
Institute for Frontier Materials (IFM)  
Deakin University  
221 Burwood Highway, Burwood Victoria  
3125, Australia  
E-mail: h.ueda@deakin.edu.au  
patrick.howlett@deakin.edu.au

[b] Dr. F. Mizuno  
Toyota Motor Corporation  
1 Toyota-cho, Toyota, Aichi  
471-8571, Japan

Supporting information for this article is available on the WWW under <https://doi.org/10.1002/batt.202200057>

© 2022 Deakin University and Toyota Motor Corporation. Batteries & Supercaps published by Wiley-VCH GmbH. This is an open access article under the terms of the Creative Commons Attribution Non-Commercial License, which permits use, distribution and reproduction in any medium, provided the original work is properly cited and is not used for commercial purposes.

are solid-state analogues of ionic liquids (ILs) and inherit advantages from their ionic nature including, low flammability, negligible vapor pressure, and high thermal and chemical stability.<sup>[12]</sup> Although the aforementioned properties enable them to be safer candidates than the other organic solid electrolytes,<sup>[13]</sup> they have been mainly used as interlayers between cathodes and anodes,<sup>[14]</sup> and not explored as ion-conductive pathways inside solid-state electrodes, except for a preliminary attempt demonstrating anode slurry preparation using an OIPC composite with agar.<sup>[15]</sup> Because ion conduction between active materials and solid electrolytes only occurs at interfaces, sufficient contact of solid electrolytes with active materials is a crucial requirement to obtain a higher rate capability<sup>[7]</sup> and longer cycle life of the electrodes, thereby making ASSBs comparable with LIBs. Indeed, as for the electrodes containing a sulfide-based solid electrolyte, it has been demonstrated that voids inside the electrodes decrease lithium-ion conduction pathways and, hence, limit the achievable capacity at each cycle.<sup>[16]</sup> In a similar fashion, this structure-property relationship would also be applicable to solid-state electrodes containing OIPCs. Therefore, studies of the interfacial structures in the electrodes dependent upon the amount of incorporated OIPCs and their relationship to the resulting battery performance will lay the foundation for the development of ASSBs.

In this paper, we report the improved charge rate capability and cyclability of solid-state graphite anodes with an increase in the amount of an OIPC composite, i.e., *N*-ethyl-*N*-methylpyrrolidinium bis(fluorosulfonyl)imide ( $[C_2\text{mpyr}][\text{FSI}]$ ) + lithium bis(fluorosulfonyl)imide (LiFSI) in the electrodes. We employed a simple electrode fabrication process; the difference from the conventional method was only the addition of the OIPC composite solution to a water-based graphite anode slurry, ensuring high applicability of this method to the roll-to-roll process. The process of solid electrolyte interphase (SEI) formation was monitored by Fourier transform infrared (FTIR) spectroscopy. Surface and cross-sectional structures of solid-state graphite anodes with various amounts of the OIPC composite were resolved by scanning electron microscopy (SEM) and thereby the effect of the incorporated OIPC composite on the charge rate capability and cyclability of the anodes was elucidated. Furthermore, elemental analysis of selected electrodes was carried out by energy-dispersive X-ray spectroscopy (EDX) to understand the dispersibility of the OIPC composite in the graphite anode. Lastly, electrochemical impedance spectroscopy (EIS) for some cycled cells was performed to correlate the difference in the battery performance with that of each resistor element as a function of the state of charge (SOC) or the depth of discharge (DOD).

## Results and Discussion

### Initial charge-discharge profile

The initial charge-discharge behavior of the solid-state graphite- $[C_2\text{mpyr}][\text{FSI}]$  composite anodes was compared with that of

an equivalent graphite anode using a liquid electrolyte, i.e., 1.0 M LiPF<sub>6</sub> in ethylene carbonate (EC)-diethyl carbonate (DEC)-dimethyl carbonate (DMC). Figure 1a shows charge-discharge profiles for the solid-state graphite- $[C_2\text{mpyr}][\text{FSI}]$  composite anode with an OIPC content of 30 wt%. As a reference, the charge-discharge profile for the graphite anode using the liquid electrolyte is also illustrated in Figure 1b. At the first charging, a peak appeared at around 0.67 V for the solid-state graphite- $[C_2\text{mpyr}][\text{FSI}]$  composite anode, which was also found for the other electrode compositions (i.e., OIPC contents of 0, 15, and 50 wt%, see Figure S1 for their charge-discharge profiles). This may be attributed to some of the origins: i) SEI formation affected by the decomposition of the  $[C_2\text{mpyr}][\text{FSI}]$  composite, ii)  $[C_2\text{mpyr}]^+$  insertion into graphite, and iii) massive decomposition of a component that does not contribute to SEI formation. Graphite/Li half cells containing  $[\text{FSI}]^-$  anions in a liquid electrolyte show a large irreversible capacity during the first charge and present a shoulder in their charge profile at 0.2–1.5 V.<sup>[17]</sup> In contrast, it has been reported that the graphite anode in a bis(trifluoromethylsulfonyl)imide ( $[\text{TFSI}]^-$ )-based IL with *N*-methyl-*N*-propylpyrrolidinium ( $[C_3\text{mpyr}]^+$ ) and Li<sup>+</sup> cations exhibits reversible intercalation of  $[C_3\text{mpyr}]^+$  cations at 0.4–0.7 V.<sup>[18]</sup> In our case, the characteristic peak was observed only in the first charging step and the charge-discharge profiles for subsequent cycles were almost identical to that of the graphite anode with the liquid electrolyte (Figures 1a vs. b at the second and third cycles). Therefore, the origin of the peak might not be due to  $[C_2\text{mpyr}]^+$  insertion into graphite. Further evidence to support this claim is the stability of graphite intercalation compounds (GICs) with pyrrolidinium cations, where small pyrrolidinium cations with a volume of  $<0.2 \text{ nm}^3$  (including  $[C_2\text{mpyr}]^+$ ) cannot form stable GICs.<sup>[19]</sup> As demonstrated in Figure 1a, the SEI formed after the OIPC decomposition provides good reversibility of lithium-ion intercalation/deintercalation processes, which is likely to be due to the presence of  $[\text{FSI}]^-$  anions. A previous report suggested that  $[\text{FSI}]^-$  anions contribute to the formation of a stable SEI showing effective passivation against both co-intercalation and cathodic decomposition of IL cations.<sup>[20]</sup> Of the ions in the OIPC,  $[\text{FSI}]^-$  anions are expected to be the main contributor to SEI formation because bond cleavage in the anions of  $[\text{TFSI}]^-$  and  $[\text{FSI}]^-$ -based ILs has been widely revealed by X-ray photoelectron spectroscopy and FTIR spectroscopy.<sup>[21]</sup> However, it should be noted that  $[C_2\text{mpyr}]^+$  cations could also be partly decomposed during the first charge. This consideration is supported by the fact that, in a similar system (i.e., *N*-butyl-*N*-methylpyrrolidinium bis(trifluoromethylsulfonyl)imide,  $[C_4\text{mpyr}][\text{TFSI}]$ ), the fragmentation of  $[C_4\text{mpyr}]^+$  cations, which is mainly the detachment of butyl side chains from the pyrrolidinium rings, precedes the  $[\text{TFSI}]^-$  breakdown during the cathodic scan.<sup>[22]</sup> The fragmentation of  $[C_2\text{mpyr}]^+$  is expected to occur at around 1.2 V vs. Li/Li<sup>+</sup>, which is within the operating voltage range (0.005–1.5 V). This potential value was calculated based on the reduction potential of  $[C_3\text{mpyr}][\text{FSI}]$ , −2.06 V vs. ferrocene/ferrocenium (Fc/Fc<sup>+</sup>)<sup>[23]</sup> and the redox potential of Fc<sup>+</sup>, 3.26 V vs. Li/Li<sup>+</sup>.<sup>[24]</sup> Section VII-(i) in the Supporting

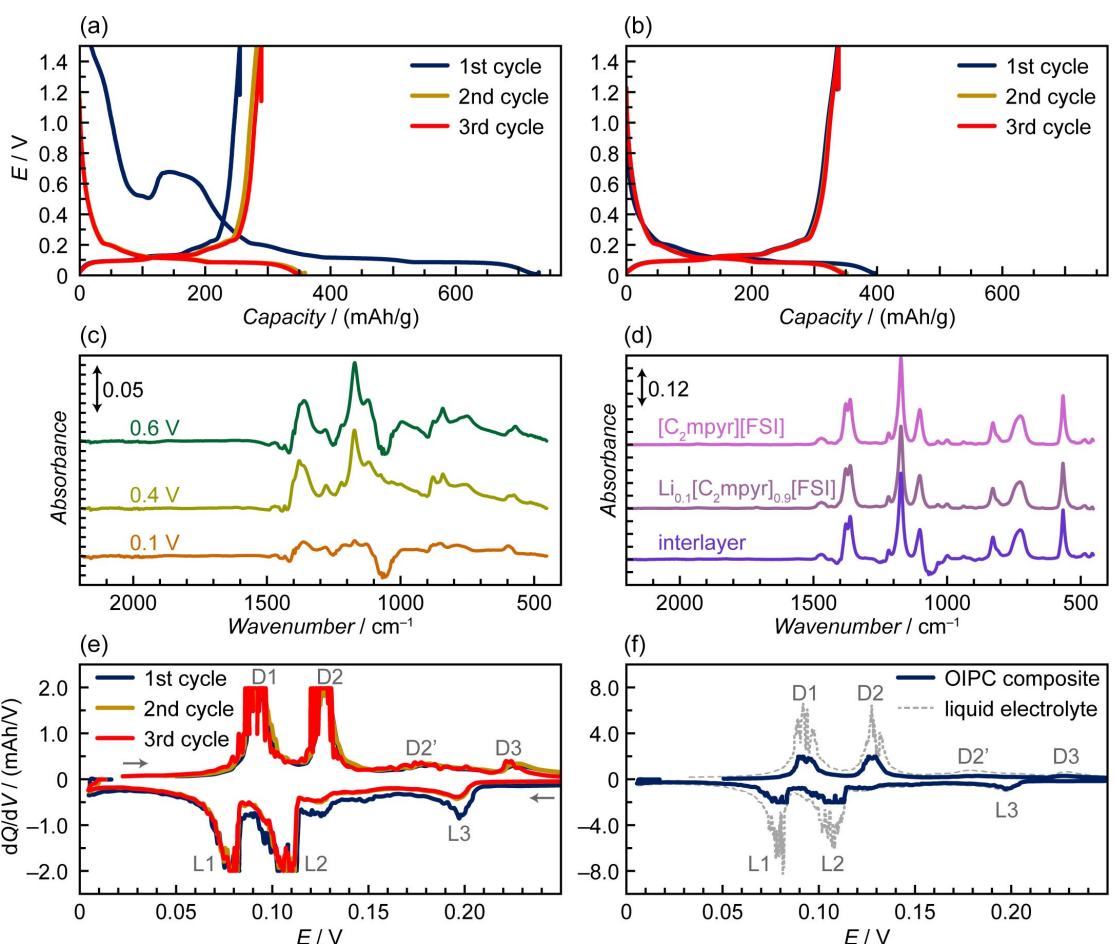


**Figure 1.** a) Charge-discharge curves for the solid-state graphite-[C<sub>2</sub>mpyr][FSI] composite anode (70 wt % graphite anode + 30 wt % [C<sub>2</sub>mpyr][FSI] composite) using the poly(vinylidene fluoride) (PVdF)-[C<sub>2</sub>mpyr][FSI] composite interlayer ([C<sub>2</sub>mpyr][FSI]-10 wt % PVdF-10 mol % LiFSI) and b) charge-discharge curves for the graphite anode with a liquid electrolyte, 1.0 M LiPF<sub>6</sub> in EC-DEC-DMC (1:1:1 volume ratio) using the Celgard 3501 (polypropylene, PP) interlayer filled with the liquid electrolyte at the first three cycles at 50 °C. c) The FTIR spectra of the solid-state graphite-[C<sub>2</sub>mpyr][FSI] composite anodes charged to 0.6, 0.4, and 0.1 V. d) The FTIR spectra of [C<sub>2</sub>mpyr][FSI], the [C<sub>2</sub>mpyr][FSI] composite ([C<sub>2</sub>mpyr][FSI]:LiFSI = 90:10 mol %), and the PVdF-[C<sub>2</sub>mpyr][FSI] composite interlayer. e) dQ/dV curves for the solid-state graphite-[C<sub>2</sub>mpyr][FSI] composite anode (70 wt % graphite anode + 30 wt % [C<sub>2</sub>mpyr][FSI] composite) at the first three cycles at 50 °C. f) Comparison of dQ/dV curves for a) and b) at the first cycle at 50 °C.

Information provides detailed insights into the appearance of the peak in the charge-discharge profiles at the first cycle.

To further analyze SEI formation at the first charging, FTIR spectroscopy was performed for the surfaces of the solid-state graphite-[C<sub>2</sub>mpyr][FSI] composite anodes (70 wt % graphite anode + 30 wt % [C<sub>2</sub>mpyr][FSI] composite). Figure 1c shows the FTIR spectra of the anodes after charging from the open-circuit voltage to the various voltages. In addition, the FTIR spectra of the interlayer, [C<sub>2</sub>mpyr][FSI] composite, and pure [C<sub>2</sub>mpyr][FSI] are illustrated in Figure 1d. As shown in Table S1, the peak wavenumbers for the spectra of the interlayer and [C<sub>2</sub>mpyr][FSI] composite are almost the same as those of [C<sub>2</sub>mpyr][FSI]. In contrast to the FTIR spectrum of the composite composed of PVdF nanoparticles and [C<sub>2</sub>mpyr][FSI],<sup>[25]</sup> no obvious peak shifts are observed for the spectrum of the interlayer. This is due to the low weight ratio of PVdF (10 wt %) in the interlayer. The shape of the spectrum for the solid-state graphite-[C<sub>2</sub>mpyr][FSI] composite anode was changed from that for the as-prepared anode before contacting with the interlayer (Figures 1c vs. S2a), and became similar to the spectrum for the interlayer. The

result suggests that the volume of the [C<sub>2</sub>mpyr][FSI] composite covering graphite particles increased after the half-cell operation. For most of the peaks, the anode charged to 0.6 V indicated weaker absorbance than the interlayer. This anode also showed blueshifts for some of the peaks originating from [FSI]<sup>-</sup> and the appearance of a new peak at 1279 cm<sup>-1</sup> (for details of the band assignments, see Table S2). Those changes in the spectrum provide evidence that [FSI]<sup>-</sup> contributes to SEI formation. Unexpectedly, a further charge of the anode to 0.4 V, which corresponds to the characteristic feature in the voltage profile at the first charging (Figure 1a), did not induce any significant change in the spectrum, except for the blue-shifted peaks at 754 and 574 cm<sup>-1</sup>. This implies that SEI formation is not the main origin of the characteristic feature. Indeed, as an alternative origin, the decomposition of PVdF in the interlayer periphery in contact with the two coin-cell spacers was confirmed after disassembling the half cell charged to 0.4 V (for details, see Section VII-(ii) in the Supporting Information). Charging the anode to 0.1 V further reduced the absorbance of the peaks stemming from both [C<sub>2</sub>mpyr]<sup>+</sup> and

[FSI]<sup>-</sup> (Table S2), suggesting the reduction of both ions. The observation of both cation- and anion-derived species by FTIR spectroscopy is supported by previous studies on similar systems using ILs with lithium metal.<sup>[21b,f]</sup> The FTIR spectra of the fully charged anode and the anode after one cycle were almost the same as that of the anode charged to 0.1 V (Figures S2b and c vs. Figure 1c). The result indicated that the essential level of SEI formation, which can prevent a drastic degradation of the components, had finished by reaching the cell voltage of 0.1 V.

Table 1 summarizes capacities and Coulombic efficiencies for the solid-state graphite-[C<sub>2</sub>mpyr][FSI] composite anodes and the graphite anode with the liquid electrolyte. The graphite/Li half cell containing the liquid electrolyte shows the first cycle Coulombic efficiency of 84.5%, whereas half cells containing the solid-state graphite-[C<sub>2</sub>mpyr][FSI] composite anodes present much lower first cycle Coulombic efficiencies (34.9%–56.5%). As stated earlier, this is due to the irreversible capacity caused by SEI formation and decomposition of PVdF in the edges of the interlayer. For all half cells, the Coulombic efficiency steadily increases with cycle number. The details for the dependence of the Coulombic efficiency and discharge capacity on the OIPC composite ratio are discussed in Section VIII-(i) in the Supporting Information. In short, a higher OIPC composite ratio (> 30 wt%) showed higher Coulombic efficiency and discharge capacity at the third cycle, which were close to those measured for the graphite anode with a liquid electrolyte. This suggests that a higher amount of the OIPC composite provides more favorable ion conduction within the anode. Surprisingly, the solid-state graphite anode without the OIPC composite could also be cycled, due to the interparticle diffusion of lithium ions as previously reported.<sup>[26]</sup> To correlate the difference in the battery performance with that in the anode structure, the results of SEM and EDX analysis are discussed later in the “Electrode structure” section.

Figure 1c shows dQ/dV curves for the solid-state graphite-[C<sub>2</sub>mpyr][FSI] composite anode with the OIPC composite ratio of 30 wt%. In addition, these dQ/dV curves are compared with those for the graphite anode with the liquid electrolyte (as a typical comparison, dQ/dV curves at the first cycle are depicted in Figure 1d). Here, we focus on the lithiation/delithiation

behavior of graphite anodes in the voltage region between 0.005 and 0.250 V. dQ/dV curves outside of this voltage region are also provided in Figure S3 to compare the difference in SEI formation and decomposition behaviors at the first charging. As can be seen in Figure 1c, three pairs of lithiation/delithiation peaks are observed at 0.080 V/0.090 V, 0.108 V/0.127 V, and 0.197 V/0.226 V, which are labeled as L1/D1, L2/D2, and L3/D3, respectively. These pairs of peaks can be assigned to phase transitions of graphite along with lithiation/delithiation. For instance, L1/D1 is due to the Stage 1/Stage 2 transition, whereas L2/D2 stems from the Stage 2/Stage 2L transition.<sup>[27]</sup> While L3/D3 is assigned to a further stage transition,<sup>[27,28]</sup> the origin of L3/D3 has been theoretically elucidated using an interaction term to include the effect of a decrease in the interaction between lithium and the graphite host lattice at low fractions of lithium intercalated into graphite (0 < x < 0.1).<sup>[29]</sup> In our dQ/dV curve (Figure 1c), an additional delithiation peak is found at 0.182 V (labeled as D2'), which is not observed for some graphites.<sup>[27–30]</sup> Although this might be related to a stage transition, the appearance of this delithiation peak depends on the types of graphite. A similar dQ/dV peak was also reported for mesocarbon microbeads (MCMB)<sup>[31]</sup> and some commercial graphites (of unspecified grades).<sup>[32]</sup> The shape of the dQ/dV curve is stable with an increase in the cycle number, except for L3, where the peak becomes broad from the first to the second cycle. A difference between the dQ/dV curves for the solid-state graphite-[C<sub>2</sub>mpyr][FSI] composite anode (30 wt% OIPC composite) and the graphite anode with the liquid electrolyte appears on the peak strengths of D2' and D3 at the first cycle. Smaller peaks are found for the solid-state graphite-[C<sub>2</sub>mpyr][FSI] composite anode, which means that lithiation/delithiation of the solid-state graphite-[C<sub>2</sub>mpyr][FSI] composite anode is not fully reversible, and a fraction of the inserted lithium remains inside the graphite. This also relates to a large irreversible capacity of the solid-state graphite-[C<sub>2</sub>mpyr][FSI] composite anode at the first cycle. The peak separations for the solid-state graphite-[C<sub>2</sub>mpyr][FSI] composite anode are estimated to be 0.010 V for L1/D1 and 0.020 V for L2/D2, which are identical to those estimated for the graphite anode with the liquid electrolyte (0.011 V and 0.019 V, respectively). The result suggests that those two phase transitions of the solid-state graphite-

**Table 1.** Charge and discharge capacities and Coulombic efficiencies at the first three cycles for the solid-state graphite-[C<sub>2</sub>mpyr][FSI] composite anodes and the graphite anode containing the liquid electrolyte.

Graphite anode : [C <sub>2</sub> mpyr][FSI] composite [wt%]	Interlayer + electrolyte	Cycle number	Charge capacity [mAh/g]	Discharge capacity [mAh/g]	Efficiency [%]
50:50	PVdF + [C <sub>2</sub> mpyr][FSI] composite	1	554.5	313.0	56.5
		2	343.0	319.4	93.1
		3	337.9	320.5	94.9
70:30	PVdF + [C <sub>2</sub> mpyr][FSI] composite	1	732.1	255.5	34.9
		2	359.3	282.4	78.6
		3	350.9	289.8	82.6
100:0	PVdF + [C <sub>2</sub> mpyr][FSI] composite	1	577.9	261.5	45.3
		2	341.6	284.5	83.3
		3	324.0	291.9	90.1
100:0	PP + 1 M LiPF <sub>6</sub> in EC-DEC-DMC (1:1:1 vol %)	1	397.8	336.2	84.5
		2	350.9	337.9	96.3
		3	346.8	338.1	97.5

[C<sub>2</sub>mpyr][FSI] composite anode occur as smoothly as those of the graphite anode with the liquid electrolyte. However, wider peak separations can be measured for the solid-state graphite-[C<sub>2</sub>mpyr][FSI] composite anode with a small amount of the OIPC composite (<15 wt%, see Figure S4). This is probably due to a relatively small contact area between the bulk OIPC composite and graphite particles in the anode, which causes a higher contact resistance, hence requiring an overvoltage to induce those phase transitions. Therefore, a higher OIPC composite ratio ( $\geq 30$  wt%) is beneficial to facilitate the phase transitions along with lithiation/delithiation. A further discussion regarding resistivity is made later in the “EIS after the cycle test” section, based on the results of EIS after the cycle test.

### Charge rate performance

Figure 2a shows charge curves at various C-rates for the solid-state graphite-[C<sub>2</sub>mpyr][FSI] composite anode with the OIPC composite ratio of 30 wt%. The plateau of the curve was shortened and blurred with an increase in the charge C-rate,

resulting in a smaller charge capacity at a higher C-rate. The same tendency was found for the other anode compositions (see Figure S5 for their charge curves) and the degree of decrease in the charge capacity with a C-rate increase was dependent on the anode composition. Figure 2b presents the charge capacity ratio at each C-rate for the solid-state graphite-[C<sub>2</sub>mpyr][FSI] composite anodes with the OIPC composite ratio of 0, 30, and 50 wt% and the graphite anode with the liquid electrolyte (see Section VIII-(ii) in the Supporting Information for the charge rate capability of the 15 wt% sample). A difference in the charge rate capability is derived from a difference in the structure inside the anode (Figure 2c). The fastest decrease in the charge capacity with an increase in the C-rate was measured for the solid-state graphite anode without the OIPC composite. This could be attributed to three reasons: i) the smallest contact area between the bulk OIPC composite and the graphite particles, ii) the relatively unstable contact between graphite particles and the copper current collector, and iii) the loss of favorable edge-edge contacts during charging. If the electrolyte/electrode contact area becomes smaller, a larger interfacial resistance will be expected. The

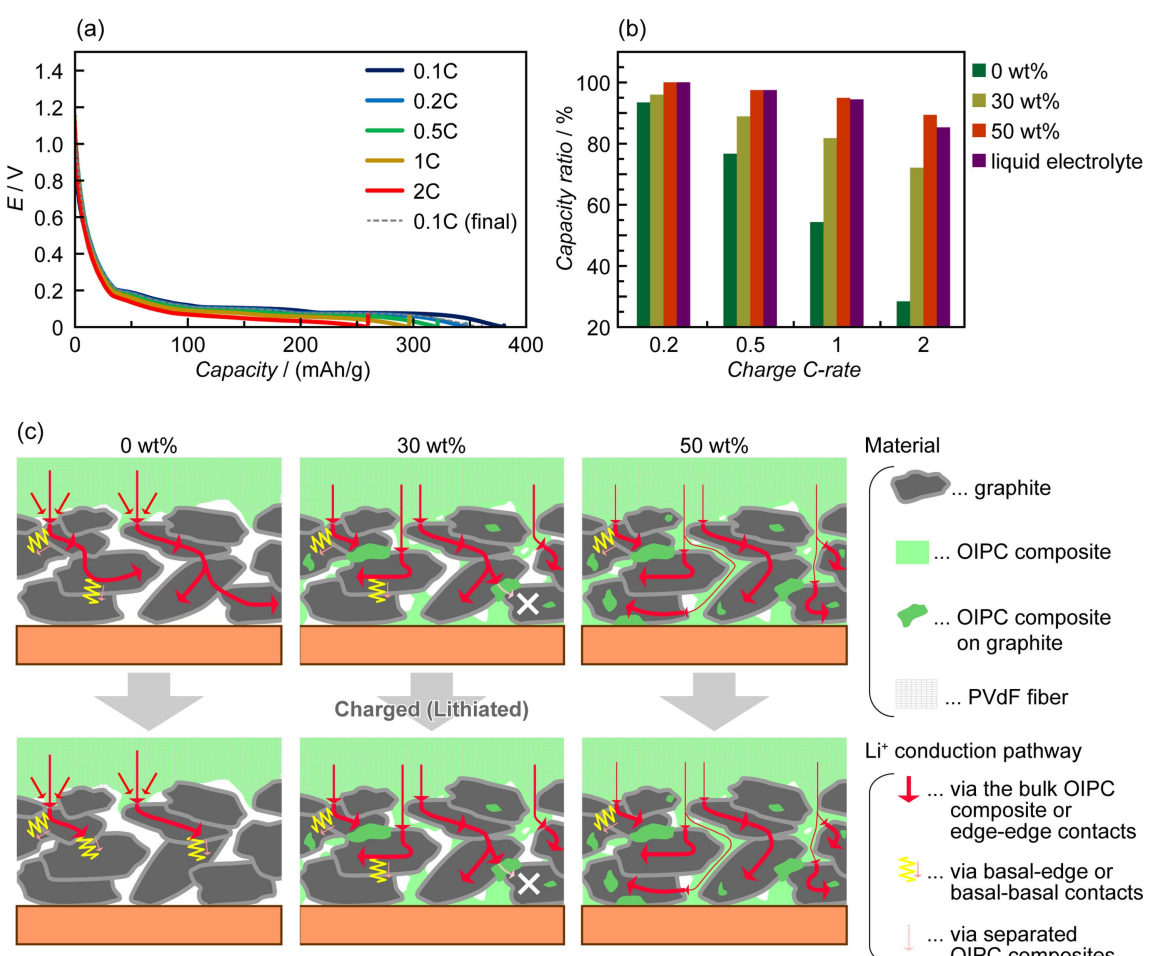


**Figure 2.** a) Charge curves for the solid-state graphite-[C<sub>2</sub>mpyr][FSI] composite anode (70 wt % graphite anode + 30 wt % [C<sub>2</sub>mpyr][FSI] composite) at various C-rates at 50 °C. b) The capacity ratio at each charge C-rate. c) The schematic illustration of the interface between PVdF fibers filled with the [C<sub>2</sub>mpyr][FSI] composite ([C<sub>2</sub>mpyr][FSI]:LiFSI = 90:10 mol %) and solid-state graphite-[C<sub>2</sub>mpyr][FSI] composite anodes with various graphite anode:[C<sub>2</sub>mpyr][FSI] composite ratios (100:0, 70:30, and 50:50 wt%).

solid-state graphite anode has no electrolyte inside and, therefore, SEI formation on the current collector is not possible. The SEI on copper is reportedly rich in organics,<sup>[33]</sup> which would enhance the adhesion of graphite particles to the current collector. However, the electrode/current collector contact in the solid-state graphite anode relies dominantly on the binder, i.e., sodium carboxymethylcellulose (Na-CMC) and van der Waals force of graphene layers with the bare substrate, which is more likely to incur the partial contact loss between graphite particles and the current collector during charging. A difference in the electrode/current collector contact will be further discussed in the “*EIS after the cycle test*” section. As for the orientation dependency of graphite particles, it is known that lithium intercalation into graphite occurs across edge planes.<sup>[34]</sup> Because defect-free basal planes of graphite particles are inactive against lithium intercalation,<sup>[35]</sup> lithium-ion conduction between graphite particles in the solid-state graphite anode without the OIPC composite is expected to take place at contact points between edge planes (red curved arrows passing through graphite particles in Figure 2c). However, if the charge rate increases, lithium intercalation via each contact point will also increase. This causes rapid volume expansion of graphite particles and could cause slippage of the contact points, changing their orientation from edge-edge contacts to unfavorable basal-edge or basal-basal contacts (shown as yellow wavy lines in Figure 2c). Such contact modification could be non-negligible because graphite particles expand by 10% along with their *c*-axes during charging from the delithiated state to the lithiated state.<sup>[36]</sup> A decrease in the charge capacity with a C-rate increase becomes less intense as the fraction of OIPC within the composite increases. This is due to the nullification of some or all of the aforementioned three adverse effects. As stated in the “*Initial charge-discharge profile*” section, an increase in the OIPC composite ratio provides graphite particles with large electrolyte/electrode contact areas, reducing the interfacial resistance. In addition, the OIPC composite plays an adhesion role in the anode, maintaining both electrolyte/electrode and electrode/current collector contacts and fastening the orientation of graphite particles at contact points. Such an adhesive feature is an inherent property of [FSI]<sup>-</sup>-based OIPCs.<sup>[37]</sup> Indeed, the OIPC composite made of 90 mol% [C<sub>2</sub>mpyr][FSI] and 10 mol% LiFSI is sticky enough to bind graphite particles. The charge rate capability increases with an

increase in the OIPC composite ratio. Importantly, the capacity ratio of the solid-state graphite-[C<sub>2</sub>mpyr][FSI] composite anodes with the OIPC composite ratio of 50 wt% (89.5% at 2C charge) is almost the same as that of the graphite anode with the liquid electrolyte (85.7% at 2C charge). This suggests that, at 50 wt%, the OIPC composite sufficiently fills the voids within the anode and covers the graphite particles to provide them with favorable lithium-ion conduction pathways from/to the bulk OIPC composite.

As demonstrated here, filling the voids in the graphite anode with the [C<sub>2</sub>mpyr][FSI] composite is beneficial to improving the charge rate capability because it can allow graphite particles to access lithium ions via the OIPC composite. Lithium-ion conduction in OIPCs has been explained by a paddle-wheel (cog-wheel) or revolving-door mechanism,<sup>[38]</sup> where the rotational motions of organic ions comprising OIPCs transfer adjacent lithium ions to the different sites in the crystal lattice. In addition, the defects (vacancies and dislocations) formed by the structural disorder in OIPCs also facilitate ion conduction.<sup>[12,39]</sup> These lithium-ion conduction mechanisms are also applicable to the case of the solid-state graphite-[C<sub>2</sub>mpyr][FSI] composite anodes. Furthermore, the [C<sub>2</sub>mpyr][FSI] composite around the graphite particles is subject to compositional change and recrystallisation followed by the formation of smaller grains (compared to the uncycled [C<sub>2</sub>mpyr][FSI] composite), as resolved for the interface between lithium-doped *N,N*-dimethylpyrrolidinium tetrafluoroborate and lithium metal after symmetric cell cycling.<sup>[40]</sup> This increases the volume of grain boundary phases that are reportedly more ion-conductive than the bulk OIPC phases.<sup>[41]</sup> The aforementioned lithium-ion conducting function of the [C<sub>2</sub>mpyr][FSI] composite and the results shown in Figure 2b deduce the positive effect of the OIPC inclusion in electrodes on the performance improvement of ASSBs.

Surprisingly, solid-state graphite-[C<sub>2</sub>mpyr][FSI] composite anodes could operate under a low volume fraction of the electrolyte (i.e., the volume fraction of LiFSI,  $\phi_{\text{electrolyte}} \leq 1.8\%$ ), which was evaluated to be  $>60\%$  smaller than that of the solid-state graphite anode with the liquid electrolyte ( $\phi_{\text{electrolyte}} = 5.0\%$ , see Table 2 for details). To obtain further insight into how much of the electrolyte per anode is required to achieve a high charge rate capability, the capacity ratio at 2C charging was plotted against  $\phi_{\text{electrolyte}}/\phi_{\text{anode}}$  in Figure 3, where

**Table 2.** Composition, volume fractions of voids ( $\phi_{\text{void}}$ ), an anode (including graphite, carbon black, and Na-CMC) ( $\phi_{\text{anode}}$ ), an electrolyte ( $\phi_{\text{electrolyte}}$ ), and a solvent ( $\phi_{\text{solvent}}$ ), and  $\phi_{\text{electrolyte}}/\phi_{\text{anode}}$ .

Aimed graphite anode : [C <sub>2</sub> mpyr][FSI] composite ratio [wt %]	Interlayer + electrolyte	$\phi_{\text{void}}$ [%]	$\phi_{\text{anode}}$ [%]	$\phi_{\text{electrolyte}}^{[a]}$ [%]	$\phi_{\text{solvent}}^{[b]}$ [%]	$\phi_{\text{electrolyte}}/\phi_{\text{anode}}$ [%]
50:50	PVdF + [C <sub>2</sub> mpyr] [FSI] composite	21.2	29.0	1.8	48.1	6.1
70:30	PVdF + [C <sub>2</sub> mpyr] [FSI] composite	35.6	37.1	1.0	26.3	2.6
85:15	PVdF + [C <sub>2</sub> mpyr] [FSI] composite	42.6	44.0	0.5	12.9	1.1
100:0	PVdF + [C <sub>2</sub> mpyr] [FSI] composite	34.1	65.9	0	0	0
100:0	PP + 1 M LiPF <sub>6</sub> in EC-DEC-DMC (1:1:1 vol%)	0 <sup>[c]</sup>	50.2	5.0	44.7	10.0

<sup>[a]</sup> Electrolyte: LiFSI or LiPF<sub>6</sub>. <sup>[b]</sup> Solvent: [C<sub>2</sub>mpyr][FSI] or EC-DEC-DMC (1:1:1 vol%). <sup>[c]</sup> All voids are assumed to be filled by 1 M LiPF<sub>6</sub> in EC-DEC-DMC (1:1:1 vol%).

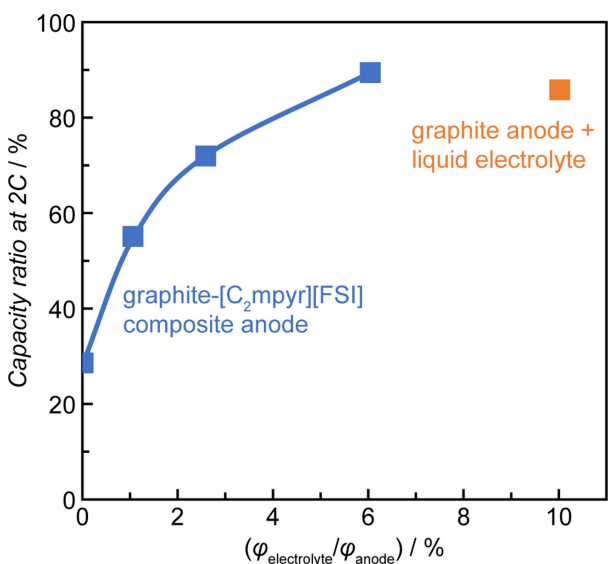


Figure 3. Plots of the capacity ratio at 2C charging vs.  $\phi_{\text{electrolyte}} / \phi_{\text{anode}}$  at 50 °C.

$\phi_{\text{anode}}$  is the volume fraction of anode, i.e., the sum of the volume fractions of graphite, carbon black, and Na-CMC. It was evaluated that the amount of the electrolyte in the OIPC composite is smaller than that in the liquid electrolyte to achieve the same charge rate capability. Specifically, the  $\phi_{\text{electrolyte}} / \phi_{\text{anode}}$  value for the solid-state graphite-[C<sub>2</sub>mpyr][FSI] composite anode with 50 wt% of the OIPC composite (6.1%) was 39% smaller than that for the solid-state graphite anode

with the liquid electrolyte (10.0%). This is one of the advantages of the transition from the conventional liquid electrolyte system to the solid electrolyte system using the OIPC composite. Owing to this transition, ca. 39% of the electrolyte volume is expected to be reduced, which would be an additional space to incorporate more graphite (and the other ingredients accordingly), thereby resulting in the improvement of the volumetric energy density (mAh/L). A possible physicochemical interpretation of a more efficient lithium-ion transfer behavior in the solid-state graphite-[C<sub>2</sub>mpyr][FSI] composite anode is discussed in Section IX in the Supporting Information.

### Cycle life

Figure 4a shows charge-discharge profiles of the solid-state graphite-[C<sub>2</sub>mpyr][FSI] composite anode with the OIPC composite ratio of 30 wt% during extended cycle testing. The corresponding dQ/dV curve for each charge-discharge profile is also illustrated in Figure 4b. The charge capacity was stable at every cycle. In contrast, the discharge capacity gradually improved as the cycle number increased and was stabilized at around the 20th cycle. This can be explained as a preconditioning process. It was reported for not only lithium/lithium symmetric cells with an OIPC composite interlayer,<sup>[40,42]</sup> but also half cells composed of a LiFePO<sub>4</sub> (LFP) cathode, an OIPC composite interlayer, and lithium metal.<sup>[42a,b,43]</sup> The preconditioning process is likely to stem from Joule heating, recrystallization of the OIPC followed by the formation of small OIPC

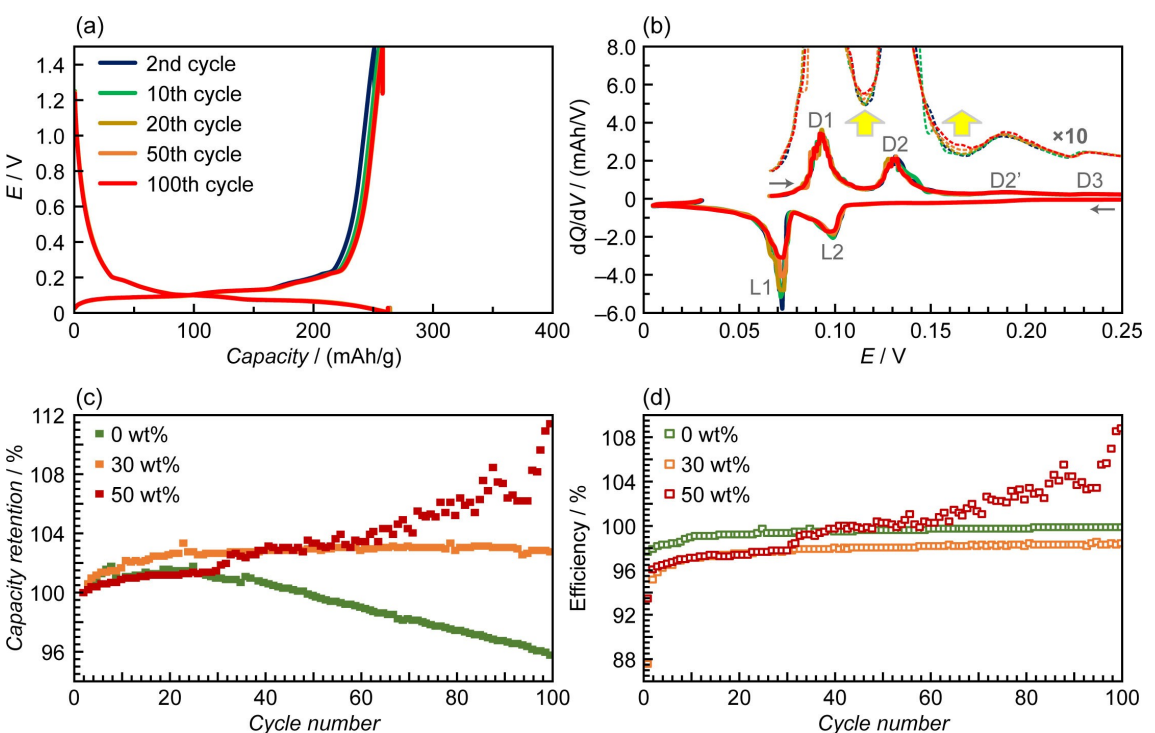


Figure 4. a) Charge-discharge curves and b) dQ/dV curves for the solid-state graphite-[C<sub>2</sub>mpyr][FSI] composite anode (70 wt% graphite anode + 30 wt% [C<sub>2</sub>mpyr][FSI] composite) at the 2nd, 10th, 20th, 50th, and 100th cycles at 50 °C. c) Capacity retention and d) Coulombic efficiency at each cycle.

grains, and the uneven concentration profile of lithium ions at the electrolyte/electrode interfaces.<sup>[42a,43a]</sup> These provide contact points with melted phases or disordered phases of the OIPC composite, and hence facilitate lithium-ion conduction. These effects are induced by cell cycling and can reduce interfacial resistance. An interesting preconditioning behavior for the solid-state graphite-[C<sub>2</sub>mpyr][FSI] composite anode is that an increase in the discharge capacity is mainly due to stage transitions higher than D1 (i.e., D2 and D2', see the enlarged curve of Figure 4b). The peak heights of these stage transitions were not changed significantly during cycling, but the discharge capacity derived from the intermediate regions (between D1, D2, and D2') gradually increased with an increase in the cycle number. The same preconditioning behavior was also observed for the solid-state graphite-[C<sub>2</sub>mpyr][FSI] composite anode with the OIPC composite ratio of 50 wt% (see Figures S6a and b for its charge-discharge profiles and dQ/dV curves during cycling, respectively). Furthermore, this anode showed an unusual dQ/dV increase at 1.0–1.5 V (Figure S7c). Because lithiation/delithiation of graphite particles occurs below 0.3 V vs. Li/Li<sup>+</sup>, this is originated from another side reaction. A possible scenario for this side reaction could be partial degradation of the PVDF fiber in the area sandwiched between the solid-state graphite-[C<sub>2</sub>mpyr][FSI] composite anode and lithium metal. This reaction may be mediated by nitrene radicals of [FSI]<sup>-</sup> decomposition products. Nitrene radicals are strong bases and can abstract H atom from C–H bonds.<sup>[44]</sup> Therefore, it is expected that they can also dehydrofluorinate PVdF. In the case of the solid-state graphite anode without the OIPC composite (see Figures S6c and d), the charge capacity was gradually increased during the first eight cycles, stabilized up to the 20th cycle, and started decreasing from the 21st cycle. It also showed the aforementioned preconditioning

behavior. However, as the decrease in charge capacity was bigger than the increase in the discharge capacity, the discharge capacity also decreased from the 21st cycle. The result suggests that the disconnection of favorable graphite-graphite contacts simultaneously progresses with preconditioning and generates more inactive graphite particles during cycling. Also, as stated in the “Charge rate performance” section, the lithium-ion conduction pathways inside the solid-state graphite anode without the OIPC composite are the most limited among the solid-state graphite anodes studied here, which could result in the fastest SEI growth at the electrolyte/electrode interfaces.

Figure 4c shows the discharge capacity retention for the solid-state graphite-[C<sub>2</sub>mpyr][FSI] composite anode with the OIPC composite ratio of 0, 30, and 50 wt% during the cycle test. Capacities, Coulombic efficiencies, and discharge capacity retention at selected cycles are tabulated in Table 3. From the first cycle to the 20th cycle, all cells displayed increases in the discharge capacity. After that, each cell presented a different plot of the discharge capacity retention. The solid-state graphite anode without the OIPC composite exhibited a steady decrease in the discharge capacity retention. Its average degradation speed was evaluated to be 0.081% per cycle, reaching a discharge capacity retention of 95.7% (275.3 mAh/g) after 100 cycles. The discharge capacity retention for the solid-state graphite-[C<sub>2</sub>mpyr][FSI] composite anode with the OIPC composite ratio of 30 wt% was stable during the cycle test (102.7%, 257.4 mAh/g at the 100th cycle). To the best of our knowledge, such a super stable discharge capacity retention of a solid-state half cell with an OIPC composite interlayer was only reported for the cell comprising an LFP cathode, the OIPC composite of 90 mol% [C<sub>2</sub>mpyr][TFSI] and 10 mol% LiTFSI, and lithium metal at 80 °C.<sup>[42b]</sup> In contrast, a

**Table 3.** Capacities, Coulombic efficiencies, and discharge capacity retention at selected cycles for the solid-state graphite-[C<sub>2</sub>mpyr][FSI] composite anodes during the cycle test.

Graphite anode: [C <sub>2</sub> mpyr][FSI] composite [wt%]	Cycle number	Charge capacity [mAh/g]	Discharge capacity [mAh/g]	Efficiency [%]	Discharge capacity retention [%]
50:50	1	301.5 <sup>[a]</sup>	281.5	93.4	–
	2	290.4	278.7	96.0	100
	10	289.8	281.0	97.0	100.8
	20	289.9	282.0	97.3	101.2
	50	287.4 <sup>[b]</sup>	288.0 <sup>[b]</sup>	100.2 <sup>[b]</sup>	103.3 <sup>[b]</sup>
	100	285.5 <sup>[b]</sup>	310.2 <sup>[b]</sup>	108.7 <sup>[b]</sup>	111.3 <sup>[b]</sup>
	101	261.4 <sup>[a,b]</sup>	329.4 <sup>[b]</sup>	126.0 <sup>[b]</sup>	–
70:30	1	295.3 <sup>[a]</sup>	258.3	87.5	–
	2	263.7	250.5	95.0	100
	10	262.5	254.6	97.0	101.6
	20	263.8	256.9	97.4	102.5
	50	263.0	257.7	98.0	102.9
	100	261.8	257.4	98.3	102.7
	101	271.1 <sup>[a]</sup>	266.9	98.4	–
100:0	1	293.8 <sup>[a]</sup>	286.6	97.6	–
	2	294.0	287.6	97.8	100
	10	293.4	290.1	98.9	100.9
	20	294.8	292.1	99.1	101.6
	50	288.0	286.6	99.5	99.7
	100	275.9	275.3	99.8	95.7
	101	300.8 <sup>[a]</sup>	300.9	100.0	–

<sup>[a]</sup> Measured at 0.1 C. <sup>[b]</sup> Affected by a side reaction.

further increase in the OIPC composite ratio to 50 wt% induced a fluctuating increase in the discharge capacity retention because of an unwanted side reaction. As for the Coulombic efficiency, a similar trend was found which also increased from the first cycle to the 20th cycle. However, the Coulombic efficiency still showed a gradual increase after the 20th cycle. For instance, the Coulombic efficiency of the solid-state graphite-[C<sub>2</sub>mpyr][FSI] composite anode with the OIPC composite ratio of 30 wt% rapidly increased from 95.0% at the second cycle to 97.4% at the 20th cycle and then further improved to 98.3% at the 100th cycle. In contrast, the Coulombic efficiency of the solid-state graphite-[C<sub>2</sub>mpyr][FSI] composite anode with the OIPC composite ratio of 50 wt% started fluctuating from the 31st cycle. The result suggests that 30 wt% is the most balanced condition in terms of charge rate capability and cycle life and a further increase in the OIPC composite ratio within the solid-state graphite-[C<sub>2</sub>mpyr][FSI] composite anode (i.e., 50 wt%) incurs the risk of fluctuation in the discharge capacity caused by a side reaction. To confirm the instability of the 50 wt% sample, another half cell with the same condition (using a different anode disk) was also cycled (Figure S8). In this case, fluctuations in the discharge capacity retention and the Coulombic efficiency were observed at an earlier cycle (i.e., the 27th cycle). Further discussion about the fluctuation in the discharge capacity retention and Coulombic efficiency for the 50 wt% sample has been provided in Section X in the Supporting Information. The systematic investigation of the effect of the incorporated OIPC composite on the charge rate capability and cycle life highlights the importance of optimizing the anode composition with an OIPC solid electrolyte to maximize cell performance.

## Electrode structure

The surfaces of the solid-state graphite anode and the solid-state graphite-[C<sub>2</sub>mpyr][FSI] composite anodes were observed by SEM. At  $\times 6,000$ , all surfaces show graphite particles partly covered by the foamy structure of carbon black (Figures 5a–c and S9a). Clear outlines of each particle were resolved for the solid-state graphite anode without the OIPC composite. As more OIPC was incorporated into the composite anode, the outlines became more blurred. This suggests that the OIPC composite covers the graphite particles and tightly connects them with each other. Therefore, a higher amount of the OIPC composite inside the anode can provide a smaller contact resistance between the bulk OIPC composite and graphite particles. Further surface analysis was carried out using a backscattered electron (BSE) detector to evaluate the dispersal of the OIPC composite in the solid-state graphite-[C<sub>2</sub>mpyr][FSI] composite anodes. In the BSE images at  $\times 6,000$  (Figures S10a–c), all anodes show grey particles, black voids, and insignificant color contrast on the resolved graphite particles, except for a few bright spots presumably because of LiFSI recrystallization. Consequently, the dispersibility of the OIPC composite is high in those regions. However, some undispersed OIPC composite grains (as light grey areas) with a diameter of up to 150  $\mu\text{m}$  and the copper current collector (as the brightest spots) are resolved in their zoomed-out images at  $\times 50$  (Figures S10d–f). The grain boundaries of OIPC composite grains are identified at  $\times 400$  for the solid-state graphite-[C<sub>2</sub>mpyr][FSI] composite anode with the OIPC composite ratio of 30 wt% (Figure S11a). Most of them form periodic grain boundaries, which are similar to those resolved for [C<sub>2</sub>mpyr][BF<sub>4</sub>].<sup>[45]</sup> Elemental mapping for this region (Figures S11b–h) confirms that the light grey areas in the BSE images are OIPC composite grains, where the

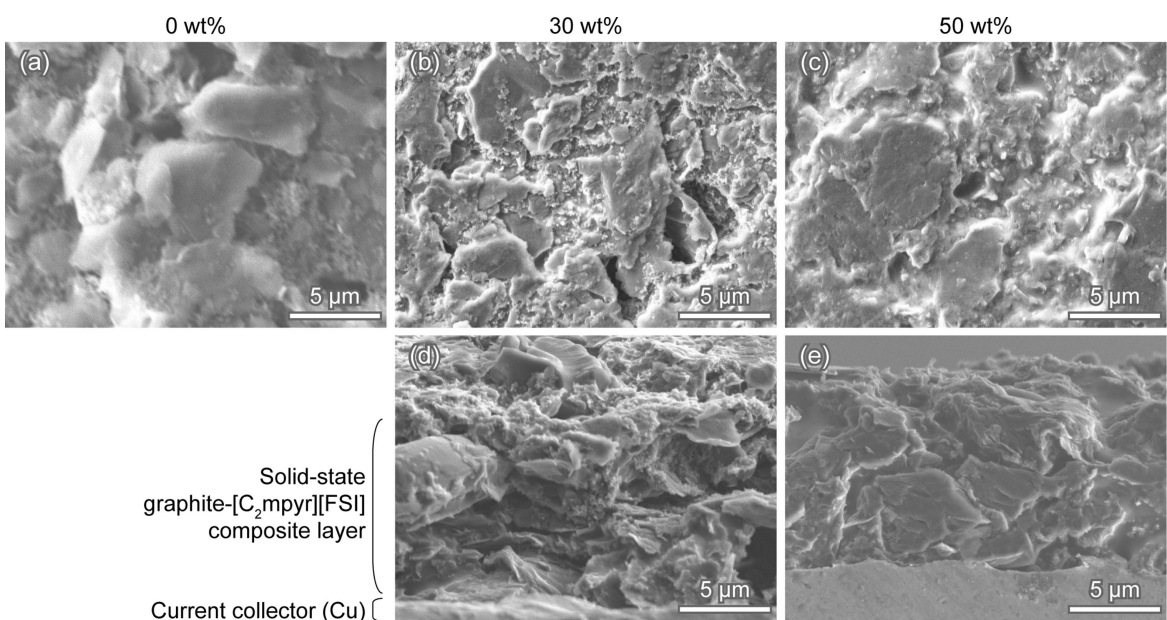


**Figure 5.** SEM images of a) the solid-state graphite anode and b–e) the solid-state graphite-[C<sub>2</sub>mpyr][FSI] composite anodes. b, d) 70 wt% graphite anode + 30 wt% [C<sub>2</sub>mpyr][FSI] composite. c, e) 50 wt% graphite anode + 50 wt% [C<sub>2</sub>mpyr][FSI] composite.

elements originated from  $[FSI]^-$  anions (i.e., N, O, F, and S atoms) are concentrated. In the other areas, these elements plus C and Na atoms are well dispersed. C atoms stem from graphite, carbon black, Na-CMC, and  $[C_2mpyr]^+$ , while Na atoms are attributed to only Na-CMC. The layered image (Figure S11b) clearly shows that the OIPC composite (S atoms) are mainly localized between graphite particles. The results indicate that the OIPC composite forms a network of lithium-ion conduction pathways inside the anode. Although the surface of the solid-state graphite- $[C_2mpyr][FSI]$  composite anodes have some undispersed OIPC composite grains, the overall anode structure appears to be homogeneous enough to evaluate the effect of the incorporated OIPC composite ratio on the half-cell performance. A comparison of the SEM images (Figures 5a–c and S9a) suggests that a higher OIPC composite ratio provides a solid-state graphite anode with better lithium-ion conduction pathways. However, because a larger amount of OIPC within the composite (i.e., 50 wt%) causes unpredictable fluctuation of the capacity during the cycle test (see the “Cycle life” section), the OIPC composite ratio is required to be fine-tuned based on gravimetric or volumetric energy density at the desired C-rate and cycle stability (e.g., 30 wt% to balance them).

The cross-sections of the solid-state graphite anode and the solid-state graphite- $[C_2mpyr][FSI]$  composite anodes were also resolved to gain further insight into their structural differences. As can be seen in Figures 5d and e and S9b, the outlines of the graphite particles become smooth with an increase in the OIPC composite ratio. In addition, more parts of carbon black are blended with the OIPC composite at a higher OIPC composite ratio. These tendencies are the same as those found in the surface images (Figures 5a–c and S9a). On the other hand, the cross-sectional images give information about the arrangement of the graphite particles. An interesting point is that graphite particles on the surface are densely packed together and face the interlayer with their basal planes, whereas inner graphite particles are randomly oriented with voids and some of them are aligned vertically to the copper current collector. This assures the efficient lithium-ion insertion/extraction of the solid-state graphite- $[C_2mpyr][FSI]$  composite anodes. Because a higher fraction of horizontally oriented graphite particles (i.e., a higher anode density) tends to decelerate lithium-ion conduction,<sup>[28,46]</sup> random orientations of inner graphite particles are beneficial. The BSE images of Figures 5d and 5e are shown in Figures S12b and c, respectively. These cross-sectional images also show homogeneously colored particles at the same observation depth, suggesting that the OIPC composite is well dispersed from the anode surface to the innermost boundary with the copper current collector. Namely, the solid-state graphite- $[C_2mpyr][FSI]$  composite anode with the OIPC composite ratio of 50 wt% clearly indicates voids filled with the OIPC.

### EIS after the cycle test

To further understand the origin of the differences in the half-cell performance between the solid-state graphite anode and

the solid-state graphite- $[C_2mpyr][FSI]$  composite anodes, EIS at various SOCs and DODs was carried out for cycled cells. Figure 6a shows the equivalent circuit used for fitting each Nyquist plot, which contains three resistances,  $R_1$ ,  $R_2$ , and  $R_3$  and a Warburg element,  $W_3$  in series and two constant phase elements (CPEs),  $Q_2$  and  $Q_3$  connected in parallel with  $R_2$  and  $R_3 + W_3$ , respectively. Fitting using this equivalent circuit was reported for not only secondary batteries with liquid electrolytes,<sup>[47]</sup> but also ASSBs.<sup>[48]</sup>  $R_1$  (hereafter denoted as  $R_{bulk}$ ) can be obtained as a high-frequency intercept and interpreted as Ohmic resistance mainly attributed to the bulk electrolyte.<sup>[47b,48b,c,49]</sup> In addition,  $R_{bulk}$  is also affected by the Ohmic resistance of the electrodes,<sup>[50]</sup> which is a more important factor for ASSBs because effective electronic/ionic conduction is one of the crucial requirements for composite electrodes in ASSBs to achieve high rate capability.<sup>[51]</sup>  $R_2$  could be assigned to the resistance of the SEI layer ( $R_{SEI}$ ), whereas  $R_3$  is derived from the charge-transfer resistance ( $R_{ct}$ ).<sup>[47a,50c]</sup>

Figures 6b and c present Nyquist plots of half cells containing the solid-state graphite anode and the solid-state graphite- $[C_2mpyr][FSI]$  composite anode with the OIPC composite ratio of 30 wt%, respectively. Experimental curves at various SOCs were well fitted by the equivalent circuit. In the case of the solid-state graphite- $[C_2mpyr][FSI]$  composite anode,  $R_{bulk}$  slightly decreased with an increase in the SOC (Figure 6d). The highest  $R_{SEI}$  was found at SOC 0% (159.2  $\Omega$ ) followed by a decrease to ca. 140  $\Omega$  at the other measured SOCs (Figure 6e).  $R_{ct}$  was 200–220  $\Omega$  at SOC < 80%, except for 136.5  $\Omega$  at SOC 9.2%, and gradually decreased from SOC  $\geq$  80% (Figure 6f). Notably, changes in  $R_{bulk}$ ,  $R_{SEI}$ , and  $R_{ct}$  values were reversible. Almost the same values were obtained during the discharging process (see Figure S13 for details of charge-discharge profiles during the EIS test and Nyquist plots at various DODs). This suggests that lithiation/delithiation of the solid-state graphite- $[C_2mpyr][FSI]$  composite anode is stable enough to provide a long cycle life. In contrast, the solid-state graphite anode without the OIPC composite exhibited fluctuations in the resistance values. While  $R_{SEI}$  seemed to be steady and reversible,  $R_{bulk}$  and  $R_{ct}$  showed sudden rises and falls in their values. For instance,  $R_{bulk}$  decreased from 48.67  $\Omega$  at SOC 23.4% to 22.39  $\Omega$  at SOC 35.1% and soared from 23.30  $\Omega$  at DOD 0% to 263.0  $\Omega$  at DOD 15.0%. Such fluctuation in  $R_{bulk}$  implies tortuous electron conduction inside the solid-state graphite anode, which could be induced by changes in either the particle/particle contact or the electrode/current collector contact during volume expansion/shrinkage of the graphite particles.<sup>[52]</sup> Contrary to lithium-ion conduction, the electron conduction between graphite particles efficiently occurs regardless of their orientations, which is due to the high electronic conductivity of graphite ( $2.0\text{--}4.0 \times 10^3$  or  $1 \times 10^4$   $S\text{cm}^{-1}$  in parallel with the basal plane and  $3.3$  or  $0.3\text{--}0.5$   $S\text{cm}^{-1}$  along the normal to the basal plane).<sup>[53]</sup> In addition, the solid-state graphite anode contains carbon black, which further develops the electron conduction pathways inside the anode. Therefore, it is estimated that the alteration of particle/particle contacts has a negligible effect on the fluctuation in  $R_{bulk}$ . However, the electrode/current collector contact

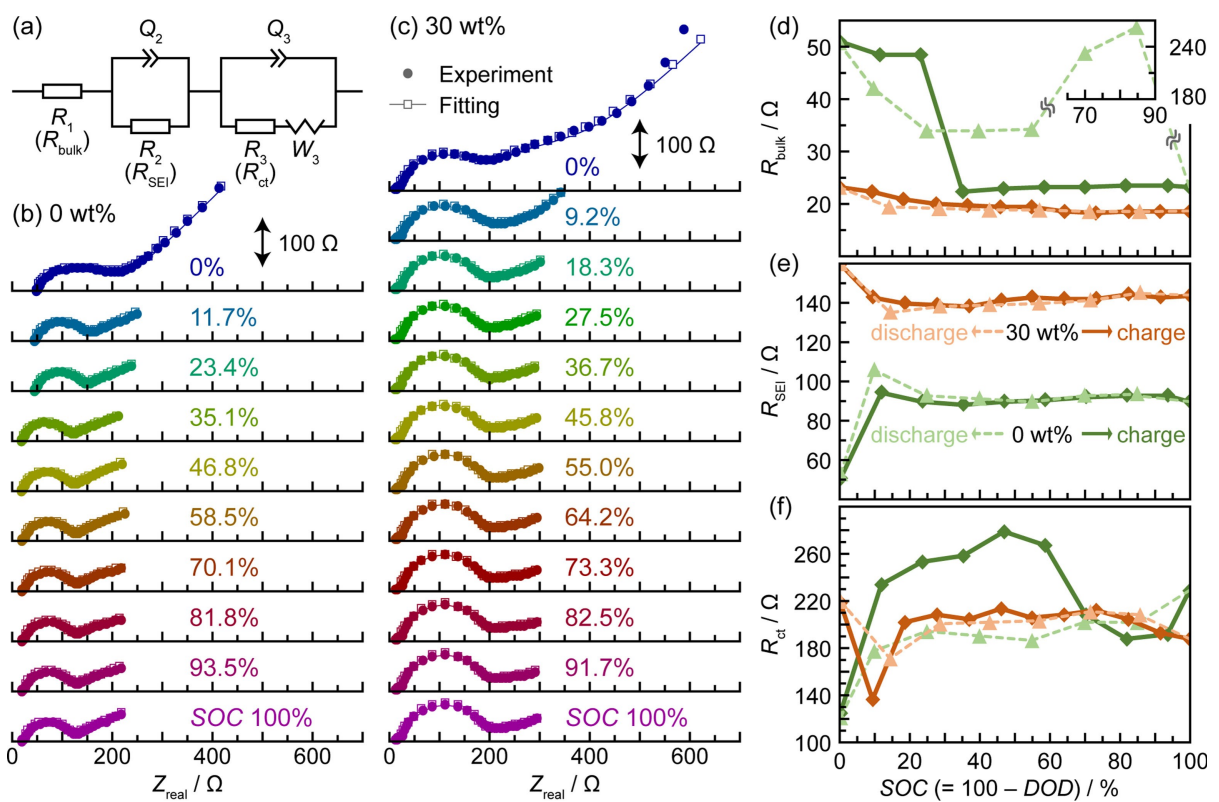


**Figure 6.** a) The equivalent circuit used for EIS fitting. Nyquist plots at various SOCs at 50 °C for the solid-state graphite-[C<sub>2</sub>mpyr][FSI] composite anodes with various graphite anode:[C<sub>2</sub>mpyr][FSI] composite ratios, b) 100:0 and c) 70:30 wt %. The plots of d)  $R_{\text{bulk}}$ , e)  $R_{\text{SEI}}$ , and f)  $R_{\text{ct}}$  as a function of the SOC or DOD.

presents a different scenario. As stated in the “Charge rate performance” section, the interaction between graphite particles and the current collector in the solid-state graphite anode is evaluated to be weaker than that of the solid-state graphite-[C<sub>2</sub>mpyr][FSI] composite anode, which is due to the absence of SEI formation and the action of the sticky OIPC composite on copper. Consequently, the solid-state graphite anode has a more unstable electrode/current collector contact than the solid-state graphite-[C<sub>2</sub>mpyr][FSI] composite anode, showing the fluctuation in  $R_{\text{bulk}}$ . As for the variation of  $R_{\text{ct}}$ , it could be elucidated as the modification of the electrolyte/electrode contact. Because the electrolyte/electrode contact area of the solid-state graphite anode is smaller than the solid-state graphite-[C<sub>2</sub>mpyr][FSI] composite anode and is localized at the outermost anode surface, the partial contact loss during volume expansion/shrinkage of the graphite particles would more severely affect the  $R_{\text{ct}}$  value. Even though  $R_{\text{ct}}$  fluctuated, it remained in the same order of magnitude as that of the solid-state graphite-[C<sub>2</sub>mpyr][FSI] composite anode. This implies that a larger fluctuation of  $R_{\text{bulk}}$  had a more impact than that of  $R_{\text{ct}}$ , which leads to the poorer charge rate capability and cycle life of the solid-state graphite anode compared to the solid-state graphite-[C<sub>2</sub>mpyr][FSI] composite anode.

Overall, the incorporation of the OIPC composite in the graphite anode not only facilitates lithium-ion conduction pathways inside the anode but also enhances the electrolyte/electrode and electrode/current collector contacts, resulting in

the improvement of charge rate capability and cycle life. This work opens up a new avenue for the development of ASSBs using an OIPC composite as an incorporated solid electrolyte within an electrode. Of course, the optimum ratio of a composite electrode differs from material to material,<sup>[51]</sup> high compatibility of the OIPC composite with the graphite anode inspires the use OIPCs in electrodes to achieve the desired cell performance. The possible benefit of using an OIPC composite as a solid electrolyte rather than using a conventional liquid electrolyte is that a high charge rate capability can be achieved with a much lower ratio of the electrolyte volume to the electrode volume. To maximize this benefit, a further reduction of the void volume in solid-state electrodes is worth performing. Because a vast number of combinations between cations and anions have yet to be studied as OIPC composites in ASSBs, identifying the effects of cation and anion chemistries on the battery performance and its root cause analysis could be the next stage of studies on such solid-state composite electrolytes. Furthermore, the positive approach shown in this study may be equally applicable to other active materials such as LFP, lithium nickel manganese cobalt oxide, sulfur, silicon etc., thereby paving the way to develop a whole new class of ASSBs.

## Conclusion

In summary, we demonstrated a promising approach to enhancing the charge rate capability and cycle life of ASSBs by incorporating the [C<sub>2</sub>mpyr][FSI] composite into a graphite anode. The effect of the OIPC composite mass ratio on the charge-discharge profile and anode structure was systematically investigated by battery tests, FTIR spectroscopy, SEM, EDX, and EIS. Half cells comprising either a solid-state graphite anode or graphite-[C<sub>2</sub>mpyr][FSI] composite anode, an electro-spun PVdF fiber interlayer filled with the [C<sub>2</sub>mpyr][FSI] composite, and lithium metal presented a relatively large irreversible capacity at the first charging, but the Coulombic efficiency gradually improved with an increased cycle number. FTIR spectra of the solid-state graphite-[C<sub>2</sub>mpyr][FSI] composite anodes after charging to the various voltages suggested that both [C<sub>2</sub>mpyr]<sup>+</sup> and [FSI]<sup>-</sup> are subject to reduction during the first charging. In addition, the post-mortem observation and FTIR spectroscopy of the inner cell components after charging to 0.4 V clarified the decomposition of PVdF in the interlayer periphery in contact with the two coin-cell spacers, which contributed to the large initial irreversible capacity. The dQ/dV analysis revealed that the lithiation/delithiation processes of the solid-state graphite-[C<sub>2</sub>mpyr][FSI] composite anode were almost the same as those of the graphite anode with a liquid electrolyte. Each dQ/dV peak separation of the solid-state graphite anode was larger than that of the anode with the OIPC composite, suggesting the incorporation of the OIPC composite in the anode reduced the interfacial resistance to facilitate the lithiation/delithiation processes. The charge rate capability was improved with an increase in the inside OIPC composite ratio and, at 50 wt%, it became competitive (the charge capacity ratio: 89.5%, 295.7 mAh/g at 2C charge) with that of the graphite anode with a liquid electrolyte (85.7%, 295.9 mAh/g at 2C charge). This improvement has been elucidated as the structural difference in the solid-state graphite-[C<sub>2</sub>mpyr][FSI] composite anodes. It was clarified that, as the amount of the OIPC composite increased, favorable lithium-ion conduction pathways were established in the anode, where graphite particles and carbon black were well covered with the OIPC composite. Although the relatively large volume fractions of voids in the solid-state graphite-[C<sub>2</sub>mpyr][FSI] composite anodes were estimated, the replacement of the conventional liquid electrolyte with the solid OIPC composite electrolyte significantly reduced the required volume fraction of the lithium salt per graphite anode to reach the same level of charge rate capability. Elemental mapping and BSE images confirmed high dispersibility of the OIPC throughout the composite anodes, except for some precipitated OIPC grains. The best cycle stability was measured for the solid-state graphite-[C<sub>2</sub>mpyr][FSI] composite anode with the OIPC composite ratio of 30 wt%. The preconditioning took ca. 20 cycles to be stabilized and, after that, the discharge capacity retention did not show an obvious decreasing trend, reaching 102.7%, 257.4 mAh/g at the 100th cycle. EIS for cycled cells highlighted the stable and reversible lithiation/delithiation processes of the solid-state

graphite-[C<sub>2</sub>mpyr][FSI] composite anode and an important role for the OIPC addition in strengthening the electrolyte/electrode and electrode/current collector contacts. The results provide useful insights into the structure-property relationship of the graphite-[C<sub>2</sub>mpyr][FSI] composite anode, which will lay a robust foundation for the development of ASSBs using OIPC composite electrodes.

## Experimental Section

### Preparation of solid-state graphite electrodes

[C<sub>2</sub>mpyr][FSI] (Boron Molecular, > 99%) was used after vacuum drying at 60 °C for > 12 h. LiFSI (Nippon Shokubai, IONEL™ LF-101) was used as received. Both [C<sub>2</sub>mpyr][FSI] and LiFSI were weighed in an Ar-atmosphere glove box (O<sub>2</sub> < 10.0 ppm, H<sub>2</sub>O < 0.1 ppm) followed by the addition of acetone (Chem-Supply, > 99.5%) outside the glove box to make a 40 wt% [C<sub>2</sub>mpyr][FSI] composite acetone solution (90 mol% [C<sub>2</sub>mpyr][FSI] and 10 mol% LiFSI). 1.2 g Na-CMC (Sigma-Aldrich, average molecular weight: 70,000 g/mol) was dissolved in 78.6 g distilled water at room temperature using a magnetic stirrer. After confirming the complete dissolution of Na-CMC in water, 1.2 g carbon black (C65, Imerys Graphite & Carbon, C-NERGY™ SUPER C65) was added to the solution followed by stirring at room temperature for > 12 h to obtain the dispersion, 1.5 wt% Na-CMC + 1.5 wt% C65 in water. Graphite (Merck, fine powder extra pure) was weighed in another vial for the electrode slurry preparation. The desired amount of the 40 wt% [C<sub>2</sub>mpyr][FSI] composite acetone solution was dropped into this vial and then, an appropriate amount of the Na-CMC + C65 dispersion was added. This graphite slurry was stirred at room temperature for > 12 h to acquire a homogenous mixture. Then, the slurry was coated onto Cu sheets (thickness: 20 µm) using a doctor blade with a wet gap of 80 µm. The solvent inside the coated slurry was evaporated in an oven at 80 °C for > 1 h. Dried sheets were punched to obtain solid-state graphite electrode disks with a diameter of 8 mm. Each disk was sandwiched by two Teflon disks (φ16 mm) followed by pressing using a pellet die (φ16 mm) at room temperature under 3,000 psi. After pressing, the weight and thickness of the electrode disks were measured. The electrode disks were further vacuum dried at 60 °C for > 12 h and used for coin cell assembly.

The compositions of the graphite anodes without the [C<sub>2</sub>mpyr][FSI] composite ([C<sub>2</sub>mpyr][FSI] + LiFSI) were aimed at 90 wt% graphite, 5 wt% C65, and 5 wt% Na-CMC. The ratios of the graphite anode to the [C<sub>2</sub>mpyr][FSI] composite were set to be (100 - x):x wt% (x = 0, 15, 30, or 50). The actual composition, electrode loading, and density of tested solid-state graphite anode disks are summarized in Table S3 in the Supporting Information. The ionic conductivity and melting point of the [C<sub>2</sub>mpyr][FSI] composite ([C<sub>2</sub>mpyr][FSI]:LiFSI = 90:10 mol%) were reported to be 7 × 10<sup>-6</sup> S cm<sup>-1</sup> (at 20 °C) and 156 °C (which was the peak temperature in the heating trace of differential scanning calorimetry, DSC, respectively.<sup>[54]</sup>

### Preparation of interlayers

Electrospun PVdF fiber was made by the procedure described in a previous paper.<sup>[54]</sup> The PVdF fiber with an Al sheet was punched into φ12.7 mm disks. The 40 wt% [C<sub>2</sub>mpyr][FSI] composite acetone solution was dropped onto those PVdF fiber disks followed by drying under an Ar atmosphere at room temperature for > 3 h.

Then, the coated PVdF fiber disks were further vacuum dried at 60 °C for >12 h. Each disk was sandwiched by two Teflon disks ( $\phi$ 16 mm) and pressed under an Ar atmosphere using a pellet die ( $\phi$ 16 mm) at room temperature under 2,000 psi. After removing Al sheets, those PVdF-[C<sub>2</sub>mpyr][FSI] composite fiber disks were used for coin cell assembly. The composition of the disks was 90 wt% [C<sub>2</sub>mpyr][FSI] composite and 10 wt% PVdF. According to the previous report, this interlayer ([C<sub>2</sub>mpyr][FSI] – 10 wt% PVdF–10 mol% LiFSI) showed an ionic conductivity of  $4.6 \times 10^{-6}$  S cm<sup>-1</sup> (at 20 °C) and two melting peaks (in the heating trace of DSC) at 130 °C for PVdF and 191 °C for the plastic crystal.<sup>[54]</sup>

### Coin cell assembly

CR2032-type coin cells were assembled in an Ar-filled glove box. Both sides of a lithium strip (Ganfeng Lithium, thickness: 50 µm) were brushed and then punched into round disks ( $\phi$ 10 mm). This brushed lithium disk was attached to a coin cell component and covered by a PVdF-[C<sub>2</sub>mpyr][FSI] composite fiber disk. Then, a solid-state graphite electrode was placed onto it. After crimping, coin cells were transferred to an oven at 50 °C and stored there for >12 h to ensure temperature equilibrium of the battery test environment.

Coin cells using a liquid electrolyte, 1.0 M LiPF<sub>6</sub> in the mixed solvent composed of EC, DEC, and DMC (EC:DEC:DMC = 1:1:1 vol%) supplied from Solvionic (99.9%, reference number: E034) were also fabricated as reference cells. In this case, instead of using a PVdF-[C<sub>2</sub>mpyr][FSI] composite fiber disk, Celgard 3501 was used as a separator. A punched separator disk ( $\phi$ 19 mm) was put on a brushed lithium disk and 200 µL of the liquid electrolyte was dropped onto the separator. After placing a graphite anode disk onto the separator, the components were crimped to assemble a coin cell.

### Battery tests

All battery tests were conducted at 50 °C using either a Neware battery cycler or a BioLogic VMP-300 potentiostat. The 1C current rate (mA) was calculated as follows: the weight of the active material for each cell (g) was multiplied by the actual discharge capacity of graphite used in this study (340 mAh/g) and then, this number was divided by 1 h. Firstly, coin cells were cycled three times using the constant-current-constant-voltage (CCCV) mode with the current rate of 0.1C for charging (lithiation) and the constant-current (CC) mode with 0.1C for discharging (delithiation). The lower and upper cut-off voltages were 0.005 V and 1.5 V, respectively. The cut-off current rate for the CV charging was 0.05C and the rest time between charging and discharging was 10 min.

After three cycles, the charge rate test was performed at 50 °C. Specifically, the test condition was the same as that of the first three cycles, except for the test mode and the current rate at each charging. The CC mode was used and the charge current rate was changed every cycle in the following order: 0.1C → 0.2C → 0.5C → 1C → 2C → 0.1C (six cycles in total). The charge rate capability was evaluated as the ratio of the charge capacity at a higher C-rate (> 0.1C) to that measured at the final 0.1C-CC charging.

After the charge rate test, the selected cells were further cycled at 50 °C. To check the capacities, the cells were initially cycled at 0.1C-CC. Then, the cells were tested at 0.2C-CC charging and 0.1C-CC discharging for 99 cycles. Finally, the capacities after the cycle test were measured at 0.1C-CC. The cut-off voltages and the rest time were the same as those of the first three cycles.

### FTIR spectra analysis

PerkinElmer IR 101820 series spectrometer with the software (v. 10.4.4) was used for attenuated total reflection (ATR)-FTIR. The spectra were taken from the solid-state graphite-[C<sub>2</sub>mpyr][FSI] composite anodes after the initial charging to 0.6, 0.4, 0.1, or 0.005 V or the first cycle at 0.1C followed by the disassembly of the coin cells in the Ar-filled glove box. The anodes were not washed after disassembly to maintain the conditions of their surfaces. An electrode sample was placed on a holder stage and sealed with an O-ring to avoid exposure of the sample to the air. The spectra in the mid-IR range from 4000 to 450 cm<sup>-1</sup> were measured for 32 scans using a diamond ATR crystal at room temperature.

### Structural analysis

SEM was carried out for selected solid-state graphite anodes using a JSM IT 300 series microscope. The cross-sections of the electrodes were obtained using razor blades. Specifically, the electrode was sandwiched between two plastic films and fixed in a holder. Then, it was cut from the electrode surface to the copper current collector while keeping contact between the electrode and the fresh edge of the razor blade. All samples were prepared in a glove box and transferred to the SEM observation room using an air-sensitive holder. Elemental analysis of the electrodes was performed by means of EDX with an Oxford X-Max 50 mm<sup>2</sup> EDX detector.

### Impedance analysis

EIS was performed at 50 °C for some cycled cells using a BioLogic VMP-300 potentiostat. The data were obtained from 1 MHz to 100 mHz with a voltage amplitude of 10 mV. To obtain the spectra at various SOCs, the cells were charged from SOC 0% at 0.1 C for 1 h and then rested for 6 h to stabilize the voltage change. After the rest period, EIS was measured for each cell. This charge and rest procedure was repeated until the cell voltage reached 0.005 V. EIS at SOC 100% was also measured after the rest time of 6 h. Similarly, the spectra at various DODs were acquired after every 0.1C discharge for 1 h followed by 6 h rest, where the final cut-off voltage at DOD 100% was 1.5 V. EIS fitting based on an equivalent circuit was carried out using the EC-Lab software (Z Fit v. 10.39).

### Acknowledgements

This work was supported under the Linkage Project [grant number: LP180100674] by the Australian Research Council (ARC). H.U., R.K., M.F., and P.C.H. acknowledge Toyota Motor Corporation (Japan) for its financial support. In addition, this research was undertaken in part at the Battery Technology Research and Innovation Hub (BatTRI-Hub) at Deakin University. We would like to thank Dr. Xiaoen Wang for the preparation of electrospun PVdF fibers. Open access publishing facilitated by Deakin University, as part of the Wiley - Deakin University agreement via the Council of Australian University Librarians.

### Conflict of Interest

The authors declare no conflict of interest.

## Data Availability Statement

The data that support the findings of this study are available from the corresponding author upon reasonable request.

**Keywords:** all-solid-state batteries · graphite · intercalations · lithiation · organic ionic plastic crystals · secondary batteries · solid electrolytes

- [1] D. Zhang, X. Xu, Y. Qin, S. Ji, Y. Huo, Z. Wang, Z. Liu, J. Shen, J. Liu, *Chemistry* **2020**, *26*, 1720–1736.
- [2] a) X. N. Penisa, M. T. Castro, J. D. A. Pascasio, E. A. Esparcia, O. Schmidt, J. D. Ocon, *Energies* **2020**, *13*, 5276; b) I. Y. L. Hsieh, M. S. Pan, W. H. Green, *Energy Policy* **2020**, *144*, 111654.
- [3] a) A. Kim, S. Woo, M. Kang, H. Park, B. Kang, *Front. Chem.* **2020**, *8*, 468; b) D. H. S. Tan, A. Banerjee, Z. Chen, Y. S. Meng, *Nat. Nanotechnol.* **2020**, *15*, 170–180.
- [4] a) R. Bisschop, O. Willstrand, F. Amon, *Fire Safety of Lithium-Ion Batteries in Road Vehicles*, RISE Report, RISE Research Institutes of Sweden AB, **2019**, 50; b) F. Larsson, P. Andersson, B.-E. Mellander, *Batteries* **2016**, *2*, 9.
- [5] a) J. Schnell, T. Günther, T. Knoche, C. Vieider, L. Köhler, A. Just, M. Keller, S. Passerini, G. Reinhart, *J. Power Sources* **2018**, *382*, 160–175; b) A. Sakuda, *J. Ceram. Soc. Jpn.* **2018**, *126*, 675–683.
- [6] a) Y.-S. Hu, *Nat. Energy* **2016**, *1*, 16042; b) P. Hovington, M. Lagace, A. Guerfi, P. Bouchard, A. Manger, C. M. Julien, M. Armand, K. Zaghib, *Nano Lett.* **2015**, *15*, 2671–2678.
- [7] H. Sato, J. Piao, H. Ueda (DARE Japan Inc.), WO 2021/075420 A1, **2021**.
- [8] A. Sakuda, T. Takeuchi, H. Kobayashi, *Solid State Ionics* **2016**, *285*, 112–117.
- [9] F. Han, J. Yue, C. Chen, N. Zhao, X. Fan, Z. Ma, T. Gao, F. Wang, X. Guo, C. Wang, *Joule* **2018**, *2*, 497–508.
- [10] J. Schnell, H. Knörzer, A. J. Imbsweiler, G. Reinhart, *Energy Technol.* **2020**, *8*, 1901237.
- [11] a) A. Chen, C. Qu, Y. Shi, F. Shi, *Front. Energy Res.* **2020**, *8*, 571440; b) S. Li, S. Zhang, L. Shen, Q. Liu, J. Ma, W. Lv, Y. He, Q. Yang, *Adv. Sci.* **2020**, *7*, 1903088.
- [12] A. Basile, M. Hilder, F. Makhlooghiazad, C. Pozo-Gonzalo, D. R. MacFarlane, P. C. Howlett, M. Forsyth, *Adv. Energy Mater.* **2018**, *8*, 1703491.
- [13] X. Wang, R. Kerr, F. Chen, N. Goujon, J. M. Pringle, D. Mecerreyes, M. Forsyth, P. C. Howlett, *Adv. Mater.* **2020**, *32*, 1905219.
- [14] a) F. Nti, H. Ueda, C. S. M. Kang, G. W. Greene, J. M. Pringle, H. Zhu, P. Howlett, M. Forsyth, X. Wang, *J. Phys. Chem. C* **2022**, *126*, 3839–3852; b) H. Zhu, D. R. MacFarlane, J. M. Pringle, M. Forsyth, *Trends Chem.* **2019**, *1*, 126–140.
- [15] S. Li, Z. Geng, L. Liu, L. Wang, Q. Su, W. Liao (Shanghai Electric Group Co., Ltd.), CN 113140787 A, **2021**.
- [16] a) M. Otoyama, H. Kowada, A. Sakuda, M. Tatsumisago, A. Hayashi, *J. Phys. Chem. Lett.* **2020**, *11*, 900–904; b) D. Hlushkou, A. E. Reising, N. Kaiser, S. Spannenberger, S. Schlabach, Y. Kato, B. Roling, U. Tallarek, *J. Power Sources* **2018**, *396*, 363–370.
- [17] a) F. Xu, C. Liu, W. Feng, J. Nie, H. Li, X. Huang, Z. Zhou, *Electrochim. Acta* **2014**, *135*, 217–223; b) S. Seki, Y. Kobayashi, H. Miyashiro, Y. Ohno, Y. Mita, N. Terada, P. Charest, A. Guerfi, K. Zaghib, *J. Phys. Chem. C* **2008**, *112*, 16708–16713.
- [18] A. Hofmann, M. Schulz, T. Hanemann, *Electrochim. Acta* **2013**, *89*, 823–831.
- [19] H. Zhang, Y. Wu, W. Sirisaksoontorn, V. T. Remcho, M. M. Lerner, *Chem. Mater.* **2016**, *28*, 969–974.
- [20] M. Ishikawa, T. Sugimoto, M. Kikuta, E. Ishiko, M. Kono, *J. Power Sources* **2006**, *162*, 658–662.
- [21] a) J. He, Y. Gu, W. Wang, J. Wang, Z. Chen, H. He, Q. Wu, J. Yan, B. Mao, *ChemElectroChem* **2021**, *8*, 62–69; b) A. Basile, A. I. Bhatt, A. P. O'Mullane, *Nat. Commun.* **2016**, *7*, 11794; c) C. Liu, X. Ma, F. Xu, L. Zheng, H. Zhang, W. Feng, X. Huang, M. Armand, J. Nie, H. Chen, Z. Zhou, *Electrochim. Acta* **2014**, *149*, 370–385; d) A. Budi, A. Basile, G. Opletal, A. F. Hollenkamp, A. S. Best, R. J. Rees, A. I. Bhatt, A. P. O'Mullane, S. P. Russo, *J. Phys. Chem. C* **2012**, *116*, 19789–19797; e) P. C. Howlett, E. I. Izgorodina, M. Forsyth, D. R. MacFarlane, *Z. Phys. Chem.* **2006**, *220*, 1483–1498; f) P. C. Howlett, N. Brack, A. F. Hollenkamp, M. Forsyth, D. R. MacFarlane, *J. Electrochem. Soc.* **2006**, *153*, A595–A606.
- [22] D. Alwast, J. Schnaitd, Y. T. Law, R. J. Behm, *Electrochim. Acta* **2016**, *197*, 290–299.
- [23] H. Ueda, S. Yoshimoto, *J. Electroanal. Chem.* **2021**, *900*, 115691.
- [24] a) R. Wibowo, S. E. Ward Jones, R. G. Compton, *J. Phys. Chem. B* **2009**, *113*, 12293–12298; b) C. O. Laoire, E. Plichta, M. Hendrickson, S. Mukerjee, K. M. Abraham, *Electrochim. Acta* **2009**, *54*, 6560–6564.
- [25] F. Nti, L. Porcarelli, G. W. Greene, H. Zhu, F. Makhlooghiazad, D. Mecerreyes, P. C. Howlett, M. Forsyth, X. Wang, *J. Mater. Chem. A* **2020**, *8*, 5350–5362.
- [26] J. Y. Kim, J. Park, M. J. Lee, S. H. Kang, D. O. Shin, J. Oh, J. Kim, K. M. Kim, Y. G. Lee, Y. M. Lee, *ACS Energy Lett.* **2020**, *5*, 2995–3004.
- [27] T.-H. Kim, E. K. Jeon, Y. Ko, B. Y. Jang, B.-S. Kim, H.-K. Song, *J. Mater. Chem. A* **2014**, *2*, 7600–7605.
- [28] J. Shim, K. A. Striebel, *J. Power Sources* **2004**, *130*, 247–253.
- [29] M. P. Mercer, M. Otero, M. Ferrer-Huerta, A. Sigal, D. E. Barraco, H. E. Hostet, E. P. M. Leiva, *Electrochim. Acta* **2019**, *324*, 134774.
- [30] a) Q. Shi, S. Heng, Q. Qu, T. Gao, W. Liu, L. Hang, H. Zheng, *J. Mater. Chem. A* **2017**, *5*, 10885–10894; b) O. Yariv, D. Hirshberg, E. Zinigrad, A. Meitav, D. Aurbach, M. Jiang, B. R. Powell, *J. Electrochim. Soc.* **2014**, *161*, A1422–A1431.
- [31] J.-H. Kim, N. P. W. Pieczonka, Z. C. Li, Y. Wu, S. Harris, B. R. Powell, *Electrochim. Acta* **2013**, *90*, 556–562.
- [32] a) M. H. Abd Elhamid, X. Xiao, M. Cai, (GM Global Technology Operations LLC), US 2015/0147641 A1, **2015**; b) X. Li, A. M. Colclasure, D. P. Finegan, D. Ren, Y. Shi, X. Feng, L. Cao, Y. Yang, K. Smith, *Electrochim. Acta* **2019**, *297*, 1109–1120.
- [33] D. Lin, Y. Liu, Y. Li, Y. Li, A. Pei, J. Xie, W. Huang, Y. Cui, *Nat. Chem.* **2019**, *11*, 382–389.
- [34] a) J. Asenbauer, T. Eisenmann, M. Kuenzel, A. Kazzazi, Z. Chen, D. Bresser, *Sustain. Energy Fuels* **2020**, *4*, 5387–5416; b) X. Yu, A. Manthiram, *Energy Environ. Sci.* **2018**, *11*, 527–543.
- [35] A. Funabiki, M. Inaba, Z. Ogumi, *J. Power Sources* **1997**, *68*, 227–231.
- [36] a) S. Schweidler, L. de Biasi, A. Schiele, P. Hartmann, T. Brezesinski, J. Janek, *J. Phys. Chem. C* **2018**, *122*, 8829–8835; b) X. Y. Song, K. Kinoshita, T. D. Tran, *J. Electrochim. Soc.* **1996**, *143*, L120–L123.
- [37] a) S. Zendegi Zelaia, Bachelor thesis, University of the Basque Country (Spain), **2019**; b) R. Yunis, D. Al-Masri, A. F. Hollenkamp, C. M. Doherty, H. Zhu, J. M. Pringle, *J. Electrochim. Soc.* **2020**, *167*, 070529; c) R. Yunis, T. W. Newbegin, A. F. Hollenkamp, J. M. Pringle, *Mater. Chem. Front.* **2018**, *2*, 1207–1214; d) J. L. McDonald, Ph.D. thesis, Deakin University (Australia), **2017**.
- [38] a) D. R. MacFarlane, M. Forsyth, *Adv. Mater.* **2001**, *13*, 957–966; b) D. Wilmer, K. Funke, M. Witschas, R. D. Banhatti, M. Jansen, G. Korus, J. Fitter, R. E. Lechner, *Physica B* **1999**, *266*, 60–68; c) L. Karlsson, R. L. McGreevy, *Solid State Ionics* **1995**, *76*, 301–308.
- [39] J. N. Sherwood, *Plastically Crystalline State: Orientationally Disordered Crystals*, Wiley-Blackwell, New York, **1979**.
- [40] L. Jin, P. Howlett, J. Efthimiadis, M. Kar, D. R. Macfarlane, M. Forsyth, *J. Mater. Chem.* **2011**, *21*, 10171–10178.
- [41] a) H. Zhu, G. Huang, L. A. O'Dell, M. Forsyth, *J. Phys. Chem. Lett.* **2021**, *12*, 9853–9858; b) W. A. Henderson, D. M. Seo, Q. Zhou, P. D. Boyle, J.-H. Shin, H. C. De Long, P. C. Trulove, S. Passerini, *Adv. Energy Mater.* **2012**, *2*, 1343–1350.
- [42] a) X. Wang, H. Zhu, G. W. Greene, Y. Zhou, M. Yoshizawa-Fujita, Y. Miyachi, M. Armand, M. Forsyth, J. M. Pringle, P. C. Howlett, *Adv. Mater.* **2017**, *2*, 1700046; b) J. Sunarso, Y. Shekibi, J. Efthimiadis, L. Jin, J. M. Pringle, A. F. Hollenkamp, D. R. MacFarlane, M. Forsyth, P. C. Howlett, *J. Solid State Electrochem.* **2012**, *16*, 1841–1848; c) P. C. Howlett, J. Sunarso, Y. Shekibi, E. Wasser, L. Jin, D. R. MacFarlane, M. Forsyth, *Solid State Ionics* **2011**, *204*, 73–79; d) P. C. Howlett, Y. Shekibi, D. R. MacFarlane, M. Forsyth, *Adv. Eng. Mater.* **2009**, *11*, 1044–1048.
- [43] a) L. Jin, P. C. Howlett, J. M. Pringle, J. Janikowski, M. Armand, D. R. MacFarlane, M. Forsyth, *Energy Environ. Sci.* **2014**, *7*, 3352–3361; b) P. C. Howlett, F. Ponzi, J. Fang, T. Lin, L. Jin, N. Iranipour, J. Efthimiadis, *Phys. Chem. Chem. Phys.* **2013**, *15*, 13784–13789.
- [44] I. A. Shkrob, T. W. Marin, Y. Zhu, D. P. Abraham, *J. Phys. Chem. C* **2014**, *118*, 19661–19671.
- [45] J. Efthimiadis, M. Forsyth, D. R. MacFarlane, *J. Mater. Sci.* **2003**, *38*, 3293–3301.
- [46] a) H. Temmyo, M. Nagayama (Panasonic Corp.), WO 2012/001840 A1, **2012**; b) W. Cui, Y. He, Z. Tang, Q. Yang, Q. Xu, F. Su, L. Ma, *J. Solid State Electrochem.* **2012**, *16*, 265–271; c) J. Shim, K. A. Striebel, *J. Power Sources* **2003**, *119*, 934–937.

- [47] a) W. Choi, H.-C. Shin, J. M. Kim, J.-Y. Choi, W.-S. Yoon, *J. Electrochem. Sci. Technol.* **2020**, *11*, 1–13; b) Q. Tang, Z. Shan, L. Wang, X. Qin, K. Zhu, J. Tian, X. Liu, *J. Power Sources* **2014**, *246*, 253–259.
- [48] a) A. Ikezawa, G. Fukunishi, T. Okajima, F. Kitamura, K. Suzuki, M. Hirayama, R. Kanno, H. Arai, *Electrochem. Commun.* **2020**, *116*, 106743; b) R. Xu, Z. Wu, S. Zhang, X. Wang, Y. Xia, X. Xia, X. Huang, J. Tu, *Chem. Eur. J.* **2017**, *23*, 13950–13956; c) R. Xu, X. Xia, X. Wang, Y. Xia, J. Tu, *J. Mater. Chem. A* **2017**, *5*, 2829–2834.
- [49] O. S. Mendoza-Hernandez, H. Ishikawa, Y. Nishikawa, Y. Maruyama, Y. Sone, M. Umeda, *Electrochim. Acta* **2014**, *131*, 168–173.
- [50] a) M. Shin, A. A. Gewirth, *Adv. Energy Mater.* **2019**, *9*, 1900938; b) P. Braun, C. Uhlmann, M. Weiss, A. Weber, E. Ivers-Tiffée, *J. Power Sources* **2018**, *393*, 119–127; c) F. Dinkelacker, P. Marzak, J. Yun, Y. Liang, A. S. Bandarenka, *ACS Appl. Mater. Interfaces* **2018**, *10*, 14063–14069; d) C. S. Sevov, K. H. Hendriks, M. S. Sanford, *J. Phys. Chem. C* **2017**, *121*, 24376–24380.
- [51] J. Park, K. T. Kim, D. Y. Oh, D. Jin, D. Kim, Y. S. Jung, Y. M. Lee, *Adv. Energy Mater.* **2020**, *10*, 2001563.
- [52] J. Illig, M. Ender, A. Weber, E. Ivers-Tiffée, *J. Power Sources* **2015**, *282*, 335–347.
- [53] a) H. O. Pierson, *Handbook of Carbon, Graphite, Diamonds and Fullerenes Processing, Properties and Applications*, Noyes Publications, Park Ridge, New Jersey, 1993; b) K. S. Krishnan, N. Ganguli, *Nature* **1939**, *144*, 667.
- [54] Y. Zhou, X. Wang, H. Zhu, M. Armand, M. Forsyth, G. W. Greene, J. M. Pringle, P. C. Howlett, *Phys. Chem. Chem. Phys.* **2017**, *19*, 2225–2234.

Manuscript received: January 31, 2022

Revised manuscript received: March 7, 2022

Accepted manuscript online: March 27, 2022

Version of record online: April 25, 2022